journal

J. Am. Ceram. Soc., 87 [11] 2033–2041 (2004)

Combustion Synthesis and Characterization of Nanocrystalline Tin and Tin Oxide (SnO_x, $x = 0–2$) Particles

D. L. Hall, A. A. Wang, K. T. Joy, T. A. Miller, and M. S. Wooldridge†

Department of Mechanical Engineering, University of Michigan, Ann Arbor, Michigan 48109-2125

Nanocrystalline SnO_x particles ($x = 0–2$) were synthesized using tetramethyltin ($Sn(CH_3)_4$) vapor as the particle precursor reactant in hydrogen/oxygen/argon (H_2/O_2/Ar) flames. The particle composition and morphology were characterized using X-ray diffractometry, transmission electron microscopy, and nitrogen (N_2) surface adsorption. By controlling the concentration of oxygen in the reactant gases and the flame temperatures, metallic tin (Sn), tin monoxide (romarchite SnO), and/or tin dioxide (cassiterite SnO_2) were generated. The crystalline powders consisted of both discrete primary particles and agglomerates, with average primary particle sizes of 23–24 nm for SnO_2 and 69 nm for Sn (based on specific surface area measurements of bulk powders collected in the exhaust region of the flame). The compositional results were interpreted using equilibrium and detailed chemical kinetics models.

I. Introduction

TIN DIOXIDE (SnO_2) is an industrially important material which is used in numerous applications where the specific electrical, optical, and mechanical properties of SnO_2 are highly desirable. For example, SnO_2 is used extensively as the active material in gas sensors,[1–7] as well as in systems where optical or electrical coatings are required, such as in low-emissivity architectural glass,[8] solar cells,[9–11] liquid crystal displays,[10,11] photodetectors,[6,11] and video touch screens,[10] to name a few. Tin monoxide (SnO) also has attractive optical and electrical properties and can be found in gas-sensing applications[12] and as anodes in lithium-ion cells.[13]

The performance of tin oxides is directly related to the particle size and compositional characteristics and consequently a strong function of the synthesis process used to generate the materials.[3,12,14] For example, SnO_2 sensor performance (e.g., stability, sensitivity, and selectivity, etc.) has been improved considerably by reducing the size of the SnO_2 particles used in the sensors[6,14–16] and/or by adding dopants (typically noble metals or other metal oxides) to the tin dioxide.[3,5,6,14,17–19] Specifically, several researchers have shown that pure SnO_2 gas-sensor performance is enhanced by using nanosized particles where the particle size is less than 10 nm.[14,15] Doped SnO_2 also exhibits improved sensor sensitivity as the crystallite size is decreased; however, at comparably larger crystallite sizes to pure SnO_2, e.g., ~15–50 nm.[15,16] Similarly, tin monoxide performance in power cell anodes is enhanced considerably by reducing the characteristic particle size.[13]

Nanosized metallic tin (Sn) is also a material of considerable interest for use in anodes of lithium-ion batteries.[20,21] Tin-based compounds have high reversible capacities; however, they can be subject to permanent loss of capacity due to decomposition on initial charging (e.g., SnO_2 decomposition into Sn and Li_2O[22]). Tin-based compounds can also experience loss in capacity after high cycling. Pure tin, tin alloys, and other tin intermetallic compounds have been proposed as alternatives to SnO_2 to eliminate issues of decomposition[22] and to improve cycling performance.[20] The performance of the tin particles is directly related to the size of the particles, where smaller, nanosized Sn facilitates rapid insertion of Li into the anode material[21] and reduces dimensional changes and potential failure in the electrodes during cycling.[20,23] In previous studies, the tin particles were typically on the order of 100–400 nm[20,22,23] in size or larger.[23]

Tin oxides can be generated using a variety of synthesis techniques including sol–gel processing,[15,18,19] chemical vapor deposition,[24] sputtering methods,[12] flame synthesis,[10,25,26] gas-phase condensation[27] and mechanochemical processing.[28] Pure tin nanopowders with particles ~100 nm or less in size can be produced by reductive precipitation.[23] Commercial production of SnO_2 powders typically uses a sol–gel technique. Sol–gel processing creates agglomerated particles with irregular particle morphologies and can lead to chlorine contamination of the powders because of the chloride particle precursors used (e.g., $SnCl_4$ and $PtCl_4$, etc.).[4] Here, we introduce a new synthesis method based on combustion of tetramethyltin (TMT, $Sn(CH_3)_4$) that can be used to generate crystalline nanoparticles of any of these three important materials: Sn, SnO, or SnO_2.

Combustion synthesis has several advantages in comparison to other nanosized particle synthesis methods. Combustion synthesis is a method that can be used to assemble sensor materials at the molecular level; thus, a large range of morphologies and compositions can be produced in one step, using one technique.[29] The technique is a continuous process as opposed to a batch process, such as sol–gel methods. The high-temperature environment is self-purifying, leading to materials with very low levels of contamination. High conversion efficiencies (i.e., reactant-to-product conversions of >90%) are readily achievable, leading to less process waste and lower pollutant emissions. Production rates can be high (>10 g/h) using laboratory-scale facilities, and combustion synthesis methods are often scalable to commercial production rates. Energy costs associated with combustion synthesis methods are also low due to the exothermic nature of the reactions.

The primary objective of the current study is to demonstrate that a robust range of material compositions and microstructures can be achieved using a single synthesis method. The approach uses the distinctive properties of a multielement diffusion burner to control the combustion characteristics known to be the most important in affecting particle properties—namely, the reactant concentrations and the combined temperature field and particle residence time.[29–31] In the following sections, the synthesis methodology is described and the results of the materials characterization studies are presented. In Discussion, the results are interpreted using combustion modeling.

Z. A. Munir—contributing editor

Manuscript No. 10285. Received June 5, 2003; approved May 25, 2004.

Based in part on the thesis submitted by D.L.H. for the M.S. Degree in mechanical engineering, University of Michigan, Ann Arbor, MI, 2001.

†Author to whom correspondence should be addressed. e-mail: mswool@umich.edu.

II. Experimental Procedure

The materials were generated using a multielement diffusion flame burner (MEDB), shown schematically in Figs. 1 and 2. Details of the burner are described in Wooldridge *et al.*,[32] and details of the TMT delivery system are provided in Hall *et al.*[33] Briefly, the 2.54-cm × 2.54-cm square burner consists of a hastalloy honeycomb support through which 173 stainless steel hypodermic needles (0.51-mm i.d.) are inserted at systematic intervals (see Fig. 2). Fuel flows through the hypodermic needles, and oxidizer flows through the remainder of the channels of the honeycomb (channel i.d., 0.81 mm). A single independent fuel tube, the secondary fuel tube (0.51-mm i.d.), is located at the center of the burner. To minimize entrainment of room air, the active area of the burner is surrounded by a shroud coflow of nitrogen (0.635 cm wide). A square optical chimney (3.8 cm × 3.8 cm × 34 cm) can also be used to extend the region of controlled reactant conditions above the burner. Particle precursor reactants can either be introduced with the fuel for the primary flame, or the precursor reactants can be injected into the center of the burner via the secondary fuel tube (see Figs. 1 and 2). In the current study, the particles were generated exclusively using the secondary fuel tube.

As indicated in Fig. 1, two flame systems are used with this synthesis method: the primary flame and the secondary flame. The fuel and oxidizer flows to the primary flame region (see Fig. 2) are independent, and no mixing of the reactants occurs within the body of the burner. Instead, mixing of the primary flame reactants occurs rapidly near the surface of the burner, and a nominally

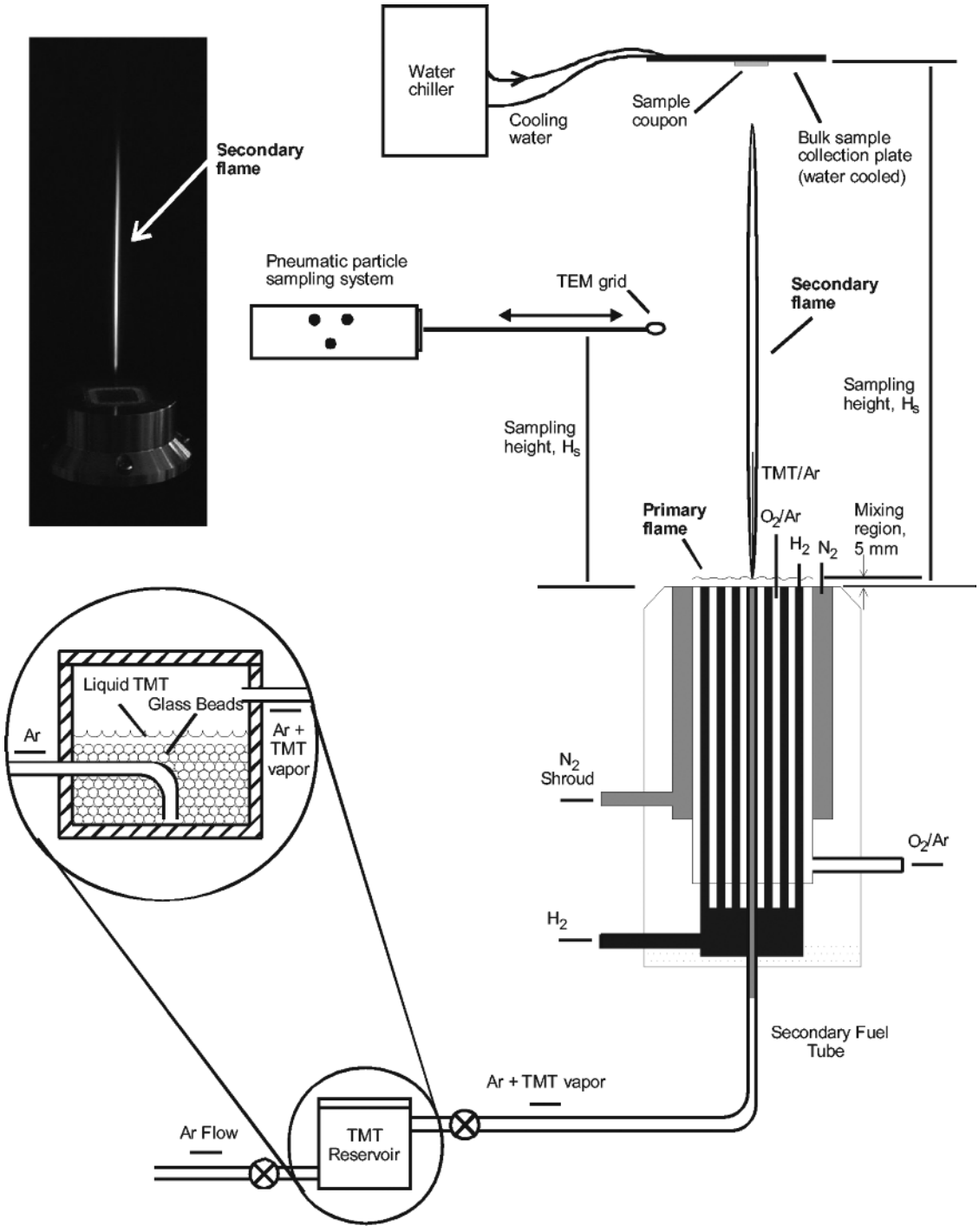

Fig. 1. Experimental schematic and photograph insert of the combustion synthesis facility used to generate the SnO_x particles. Note the $H_2/O_2/Ar$ primary flame does not emit visible radiation for the conditions studied, and the primary flame is therefore not apparent in the photograph insert.

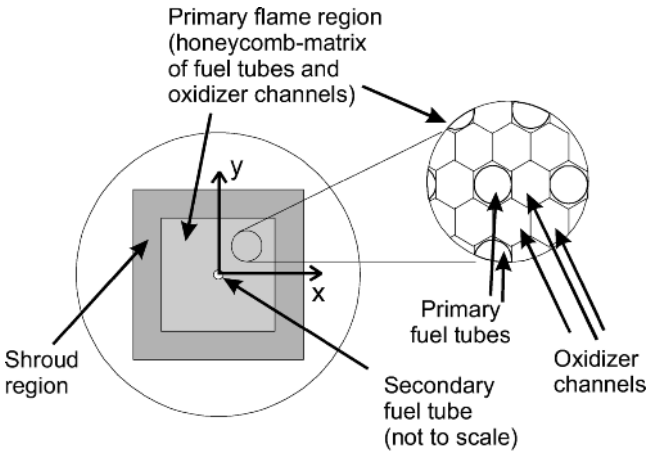

Fig. 2. Top view schematic of the multielement diffusion burner demonstrating the arrangement of the primary and secondary fuel tubes and oxidizer channels (not to scale). Critical burner dimensions are provided in the text.

uniform one-dimensional flame sheet, the primary flame, is formed (except in the immediate vicinity of the secondary fuel tube). When the particle precursor reactants are directed through the secondary fuel tube, a lifted diffusion flame, the secondary flame, is created. The primary flame has characteristics of a premixed flame for heights above the mixing region (>3–5 mm). The secondary flame is a lifted, a laminar diffusion flame (with a lift-off distance of 5 mm from the surface of the burner), where the oxidizing species are provided from the primary flame system. No particles are produced from the primary flame. All particles are produced as products of the secondary flame. The temperature profiles of the primary flame have been measured and are well-characterized by 1D "top-hat" profiles.[32] The temperature, velocity, and composition gradients of the secondary flame have not been measured due to difficulties associated with the adverse combustion conditions (high temperatures, high velocities, catalytic reaction, and particle accumulation effects) and due to difficulties with interrogating the small dimensions involved (the luminous region of the secondary flame is typically less than 6 mm in diameter).

In the current work, hydrogen (H_2, Cryogenic Gases, 99.99%) and oxygen (O_2, Cryogenic Gases, 99.995%) diluted in argon (Ar, Cryogenic Gases, 99.998%) were used to generate the primary flame. Nitrogen (N_2, Cryogenic Gases, 99.998%) was used as the shroud gas. TMT vapor diluted in argon was used as the particle precursor reactant. TMT (Alfa Aesar, 98%) vapor/Ar mixtures were generated by bubbling argon through a reservoir of liquid TMT maintained at room temperature. Vapor pressure measurements were made to confirm the argon was saturated in TMT vapor. The results indicated saturated mixtures of 21%–23% TMT dilute in Ar (mole basis) were delivered to the secondary fuel tube for all conditions studied, regardless of the argon flow rate. All reactant flow rates were monitored using calibrated rotameters or calibrated flow meters. The burner was operated at atmospheric pressure conditions ($P \cong 101$ kPa) for all experiments.

Microscopic and bulk properties of the particles were analyzed using X-ray diffraction (XRD, Rigaku rotating anode X-ray diffractometer), transmission electron microscopy (TEM, JEOL 4000EX), and surface adsorption (BET, N_2 adsorption, Micromeritics ASAP 2010 accelerated surface area and porosimetry system). Bulk samples were obtained by deposition of the particles onto sampling coupons mounted on a cold plate placed in the exhaust region of the burner. Sampling locations for the cold plate were all greater than 20 cm above the surface of the burner and typically were obtained for sample heights of $H_s = 34$ cm. Sampling times to obtain sufficient material for bulk analysis by XRD or BET analysis were typically 5–10 min. Samples for TEM analysis were obtained by rapidly inserting a probe into the secondary flame and depositing particles directly onto the TEM grids (carbon film on copper grids, Electron Microscopy Science, CF300-C450). The TEM sampling times were all less than 1 s. Additional details of the TEM sampling system are provided in Wooldridge *et al.*[32]

III. Results

(1) Composition

Table I is a summary of the experimental conditions examined and the results obtained for powder composition and material production rates. The effects of three important synthesis parameters were considered: (1) the local level of oxygen-containing species available for reaction with the $Sn(CH_3)_4$, (2) the temperature of the primary flame, and (3) the particle residence time at high temperatures. The oxygen species concentrations were controlled by changing the equivalence ratio (ϕ, the quotient of the actual fuel-to-oxygen ratio of the reactants divided by the stoichiometric fuel-to-oxygen ratio) of the primary flame. The TMT of the secondary flame was not considered in the determination of the equivalence ratio of the primary flame. The temperature of the primary flame was examined by changing the dilution level of the primary flame reactants with argon, while maintaining a constant equivalence ratio. Particle residence time/temperature effects were examined by sampling materials at various distances from the burner surface, by extending the regions of high temperatures via

Table I. Experimental Conditions and Results

Case	ϕ[†]	H_2 (L min^{-1})	O_2 (L min^{-1})	Ar (L min^{-1})	TMT/Ar (mL min^{-1})	H_s[‡] (cm)	Chimney present	Measured production rate (mg/s)	Powder color[§]	Predicted production rate (mg/s)	T_{ad}[†] (K)
1	0.75	2.94	1.95	24.44	62.6	34	Yes	0.56	W	1.42	1410
2[¶]	0.90	2.48	1.38	17.25	395	3.2/5.2[¶]	No	–	–	8.93	1590
3	0.99	2.94	1.48	11.70	64.3	34	Yes	–	G/Y	1.45	2160
4	0.99	2.96	1.50	18.82	268	25	No	–	W	6.05	1690
5	1.00	2.94	1.48	18.49	80.7	34	Yes	0.30	W	1.82	1700
6	1.00	2.94	1.48	18.49	82.7	34	Yes	0.23	W	1.87	1700
7	1.00	2.94	1.48	18.49	82.7	34	Yes	0.13	W	1.87	1700
8[¶]	1.02	5.33	2.61	14.85	395	5.2[¶]	No	–	–	8.93	2430
9	1.03	2.96	1.44	18.97	86.6	21	No	0.03	W	1.96	1650
10	1.18	2.98	1.26	17.67	30.3	34	Yes	0.33	G/Y	0.69	1560
11	1.18	2.98	1.26	12.72	64.3	34	Yes	0.29	G/Y	1.45	1880
12	1.19	3.49	1.47	18.33	60.9	34	Yes	–	G/Y	1.38	1670
13	1.20	3.50	1.47	18.33	60.9	34	Yes	–	G/Y	1.38	1670
14	1.21	3.58	1.48	18.49	60.9	30	No	0.04	W	1.38	1660
15	1.27	3.00	1.18	13.91	82.7	21	No	0.13	G/Y	1.87	1700

[†]The equivalence ratios and the adiabatic flame temperatures are based on the reactants of the primary flame and do not include fuel or argon concentrations from the secondary flame. [‡]H_s = sample height. [§]W = white; G = gray; Y = yellow/brown. [¶]Conditions used to obtain TEM samples from the secondary flame. The sampling heights were variable; however, H_s was less than 6 cm for all TEM samples.

the chimney, and by changing the flow rates of the TMT/Ar and H_2/O_2/Ar gases.

Powder composition was determined by comparison of the XRD patterns of the powder samples with accepted standards for SnO_2, SnO, and Sn. Figure 3 shows representative XRD patterns obtained in the current study for each material. The SnO_2 peaks all indexed to the tetragonal crystallographic phase of α-SnO_2 or the cassiterite form of tin dioxide. The SnO peaks indexed to the romarchite form of tin monoxide, and the Sn peaks indexed to metallic tin. Throughout the study, all XRD analyses of white powder samples indexed to SnO_2, yellow/brown powder samples indexed to SnO, and gray powder samples indexed to Sn. Therefore, the sample color (listed Table I) was considered a good indication of the material composition.

As indicated by the results shown in Table I, the most important parameters in determining the composition of the product powders were the equivalence ratio and temperature of the primary flame. For near-stoichiometric or fuel-lean operation ($\phi \leq 1.0$) at moderate temperatures (temperature effects on composition are presented below), SnO_2 was formed. For fuel-rich conditions ($\phi > 1.0$), both SnO and Sn were formed. Figure 4 is a schematic representing the results of the macroscopic composition of the powders as a function of equivalence ratio. (Note that the figure is not meant to depict the composition of individual nanoparticles.) Fig. 4 also shows the variation in composition of the bulk materials as a function of location on the sample coupon. Approximate dimensions are provided for reference on the figure. Due to the geometry of the secondary flame (i.e., the radial symmetry), the powder depositions were nonuniform in composition for the fuel-rich conditions, with lower levels of tin oxidation found near the center of the samples. Because it was difficult to isolate the Sn from the SnO samples and vice versa (due to the lack of a distinct transition from Sn to SnO on the sample coupons (see Fig. 4) and due to aerosolization of the powders on removal from the sample coupon), some Sn and SnO XRD patterns indicated small peaks attributable to the alternative material. No compositional variation

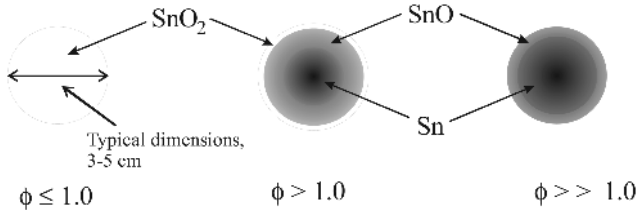

Fig. 4. Schematics indicating the compositional distribution on the sample coupon as a function of equivalence ratio (for moderate temperatures). Note the schematics are indications of the composition of the bulk materials and are not meant to represent composition of individual nanoparticles.

was observed with the $\phi \leq 1.0$ samples obtained at moderate temperatures, and no Sn or SnO peaks were identified in the SnO_2 XRD patterns.

To further examine temperature/residence time effects independent of equivalence ratio effects, experiments were performed where ϕ of the primary flame was kept constant and the argon dilution of the primary flame was altered. Reducing the argon dilution of the primary flame increases the temperature of the primary flame, while potentially simultaneously decreasing the residence time of the SnO_2 particles formed in the secondary flame (due to mixing of the primary and secondary flame gases near the surface of the burner). Increasing the temperature of the primary flame leads to added decomposition of the products of the primary flame.

Based on previous characterization studies of the MEDB including *in situ* temperature measurements using laser absorption spectroscopy and thermocouple measurements,[32,34] the maximum temperature of the primary flame, T_{ad}, can be estimated using adiabatic equilibrium calculations and the known equivalence ratio and level of argon dilution of the primary flame (for calculation

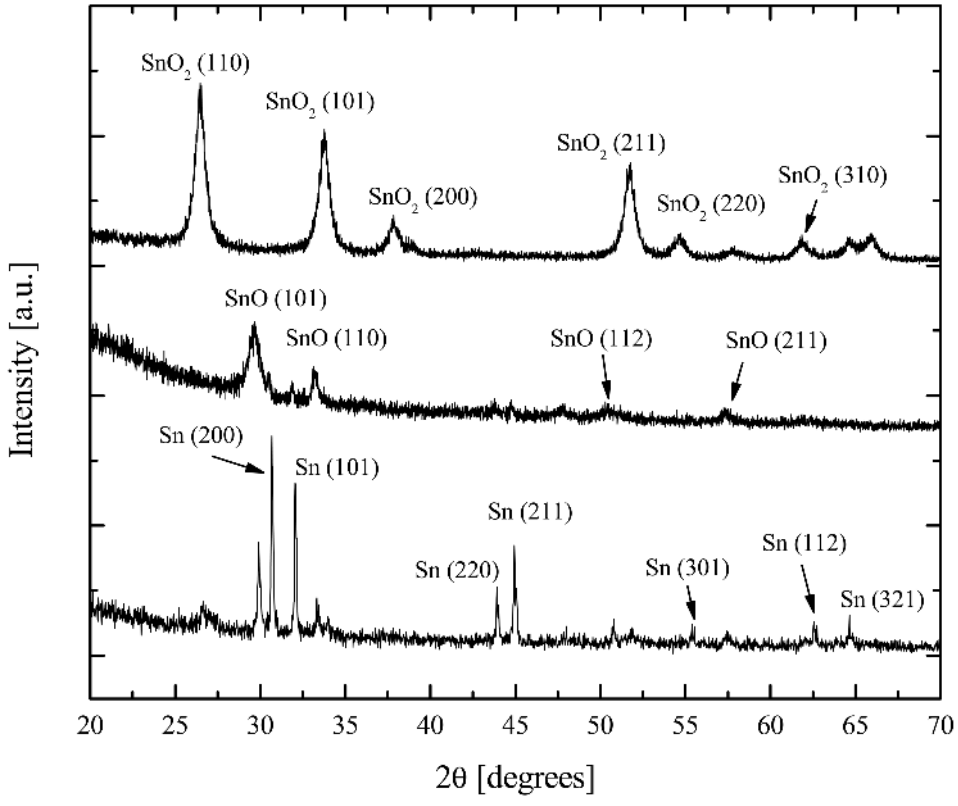

Fig. 3. Typical X-ray diffraction patterns of as-produced SnO_2, SnO, and Sn powders. The experimental conditions for each sample were as follow: SnO_2, $\phi = 1.03$, TMT/Ar = 86.6 mL min^{-1}, no chimney, $H_s = 21$ cm; SnO, $\phi = 1.19$, TMT/Ar = 60.9 mL min^{-1}, chimney, $H_s = 34$ cm; Sn, $\phi = 1.27$, TMT/Ar = 82.7 mL min^{-1}, no chimney, $H_s = 21$ cm.

details, please see Donovan *et al.*[34]). The calculated values for T_{ad} are provided in Table I as an indication of the magnitude of the changes in the primary flame temperatures examined in the study. For reference, a 37% change in the argon flow rate to the primary flame leads to a 27% change in the predicted adiabatic flame temperature.

Similar to the equivalence ratio, the temperature of the primary flame was found to be a significant factor affecting the material composition. Higher temperatures (lower argon concentrations) led to formation of Sn and SnO at $\phi = 0.99$, a condition where previously at lower primary flame temperatures only SnO_2 was produced. The change in the powder composition as the temperature of the primary flame is increased is consistent with model predictions, which are discussed below.

Changing the TMT/Ar flow rate, varying the sampling location, and/or using the chimney to affect particle residence times at high temperatures, for all cases where $\phi \leq 1.0$ and the dilution of the primary flame was moderate (i.e., primary flame temperatures were moderate), had no effect on the material composition. SnO_2 was produced in all cases (see Table I). For conditions where $\phi > 1.0$ or conditions with low dilution of the primary flame reactants (i.e., primary flame temperatures were high), if the Sn or SnO samples were not obtained before significant mixing with room air occurred, the Sn and SnO would further oxidize rapidly to form SnO_2. For example, comparing cases 14 and 15 listed in Table I (which consider approximately the same equivalence ratio, $\phi \cong 1.2$–1.3, and TMT/Ar flow rate, both without the use of the chimney) showed that sampling 9 cm higher in the exhaust region provided the particles with sufficient time at high temperatures to lead to complete oxidation of the tin. Collectively, the study of particle residence time effects indicated oxidation of the tin species occurred rapidly provided sufficient oxygen was available locally for reaction.

(2) Microstructure

The effects of burner operating conditions on particle size and morphology characteristics were also investigated. For all conditions examined in the study, the powders consisted of both discrete nanosized primary particles and particle aggregates. Figures 5 and 6 are low- and high-magnification micrograph images, respectively, of the typical particle structures observed. The crystalline nature of the particles is clearly evident (see Fig. 6), and the different lattice fringe orientations indicate sintering was relatively slow between particles.

Particle size distributions were obtained for selected TEM samples. Results for a typical fractional population for synthesis of SnO_2 nanoparticles are shown in Fig. 7. The particle size statistics were obtained using the methods described in Wooldridge *et al.*;[32] however, a larger number of particles were counted in the current work ($N > 800$), to ensure more accurate particle statistics (geometric mean particle diameters, $\bar{d}_p$, were changing by less than 3% with the incorporation of additional particle count data). In general, the geometric mean particle diameters of primary particles sampled from the secondary flame were less than 12 nm, and particle aggregates were less than 100 nm in size (maximum chord length). The particle size distributions were relatively well represented by lognormal population distributions ($R^2 = 0.9998$; see Fig. 7), and there was little variation in the particle size statistics as a function of height above the burner for the sample locations examined via TEM imaging ($H_s = 32, 52$ mm).

Specific surface area (SSA) measurements of bulk samples obtained in the exhaust region of the burner were used to estimate the average particle size of the final product materials. Values for SSA for $\phi = 0.75$, $\phi = 1.00$ (TMT/Ar = 80.7 mL min^{-1}), and $\phi = 1.19$ were 37.6, 36.2, and 15.0 m^2/g, respectively. Although the particles are not spherical (as seen in Fig. 6), to a first approximation, the average particle diameter via SSA can be determined using

$$\bar{d}_{p,SSA} = \frac{6}{SSA\rho_{(SnO_2 \text{ or } Sn)}} \quad (1)$$

Based on the compositional analysis described above, for $\phi \leq 1.0$ with moderate primary flame temperatures, the density for SnO_2 (6.85 g/cm^3)[35] is used in Eq. (1). For high-temperature conditions and/or $\phi > 1.0$, the density for Sn (5.77 g/cm^3)[35] is used. For the SSA values provided above, the values for $\bar{d}_{p,SSA}$ are 23.3 nm ($\phi = 0.75$), 24.2 nm ($\phi = 1.00$), and 69.4 nm ($\phi = 1.19$). The larger dimension for the Sn particles compared with the SnO_2 particles is consistent with the lower melting point of Sn compared with SnO_2 ($T_{mp,Sn} = 231.9$°C,[35] $T_{mp,SnO_2} = 1630$°C [35]). The Sn particles will sinter more rapidly both in the secondary flame and on the collection plate, leading to more coarse particles.

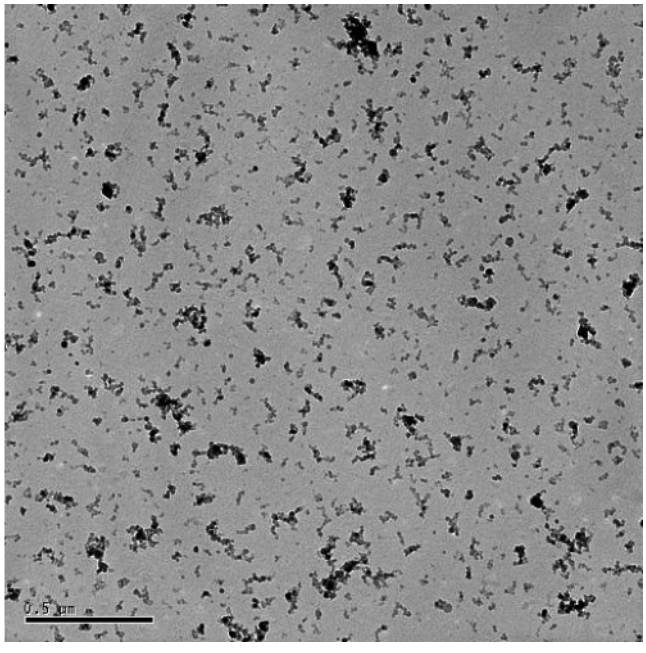

Fig. 5. Low-magnification (10K) transmission electron micrograph of particles sampled from the $H_2/O_2/Sn(CH_3)_4/Ar$ flame system: $\phi = 0.90$; TMT/Ar = 395 mL min^{-1}; $H_s = 5.2$ cm; no chimney. Size bar = 500 nm.

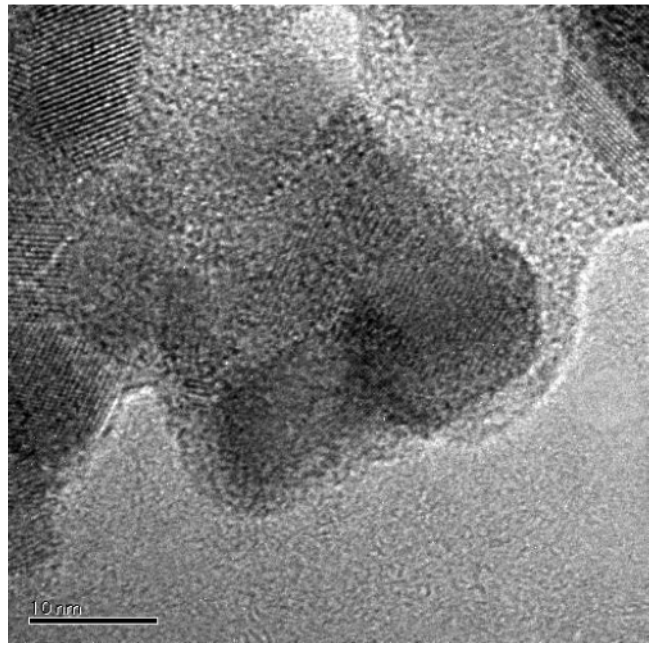

Fig. 6. High-magnification (500K) transmission electron micrograph of particles sampled from the $H_2/O_2/Sn(CH_3)_4/Ar$ flame system: $\phi = 1.02$; TMT/Ar = 395 mL min^{-1}; $H_s = 5.2$ cm; no chimney. Size bar = 10 nm.

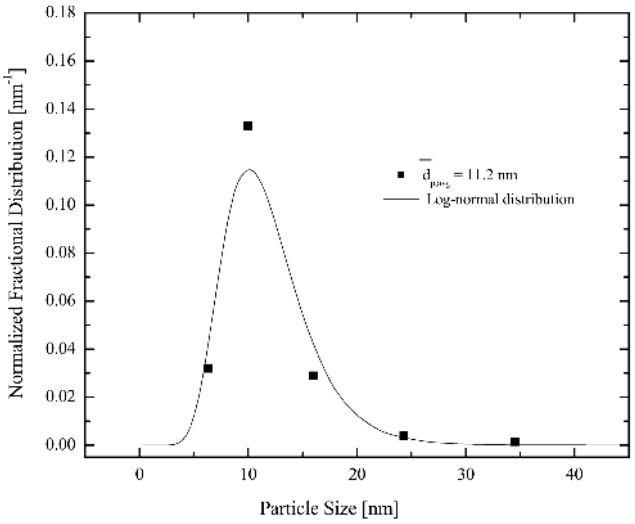

Fig. 7. Fractional size distribution of particles obtained from TEM images of samples taken at $\phi = 0.90$, TMT/Ar = 395 mL min^{-1}, and no chimney.

The particle sizes determined using BET are larger than those determined using TEM imaging; which is consistent with the respective sampling conditions. The BET and TEM particle sizes were obtained at dramatically different particle sampling times and sampling locations. The BET samples, which yielded larger particle sizes of $\bar{d}_{p,SSA}$ = 23–24 nm for SnO_2, were obtained from the exhaust region of the burner (i.e., longer residence times) using comparatively long sampling times (minutes). The TEM samples, which yielded smaller particle sizes of $\bar{d}_{p,TEM}$ = 10–12 nm for SnO_2, were obtained directly from the secondary flame using very short sampling times (<1 s).

Although particle sizes determined by SSA are inherently larger than those determined by TEM imaging when necking and bridging occurs between primary particles,[36] a comparison of the TEM and BET results for SnO_2 indicates that either significant particle growth is occurring in the secondary diffusion flame or significant particle restructuring is occurring on the sampling coupon on the cold plate. Therefore, the BET results for particle size represent an upper limit to the dimensions of the particles produced using the operating conditions presented in Table I, and the TEM results represent an approximate lower limit (assuming the particles could be rapidly quenched without the occurrence of significant particle restructuring).

(3) Mass Production

Mass production rates were measured for several samples to provide an indication of the potential manufacturing rates achievable (see Table I). The corresponding maximum predicted production rates based on the known TMT/Ar flow rates and saturation levels (assuming 100% conversion efficiency) were also determined (see Table I). All the experimental values were significantly below the predicted values. However, the differences were not likely due to low reactant-to-product conversion efficiencies, as much as due to the low collection efficiency of the bulk sampling method used. Material could bypass the cold plate and/or deposit on the cold plate outside the sample coupon region. Although the particle production rates were low compared with commercial powder production methods, the MEDB synthesis technique was not optimized for maximum production rates. In addition, the synthesis approach can be scaled to increase production rates by increasing the *x*–*y* dimension of the burner and incorporating additional secondary fuel tubes into the honeycomb matrix of the primary flame. Although the optimal spacing of the additional secondary fuel tubes would require additional study (to identify potential interactions between the particle-producing flames), preliminary results indicate a spacing of 1.25 cm between secondary fuel tubes would be sufficient.

IV. Discussion

The results for composition and particle morphology are interpreted using chemical kinetic and equilibrium models of the synthesis environment. Previously, we had obtained good agreement between one-dimensional premixed modeling of the primary flame (not including the effects of the secondary flame) and measured radical profiles by incorporating detailed chemical kinetics in the model simulations.[34] While the 1D premixed model does not accurately describe the mixing conditions in the first few millimeters above the burner surface, the results can be used to infer trends about the conditions of the primary flame system above (i.e., downstream of) the initial mixing region. Figure 8 shows the model results for the minor and major species of the primary flame for a typical stoichiometric condition. The temperature profile used in the model is a polynomial fit to a measured temperature profile of the primary flame system when the secondary fuel tube was not used for particle

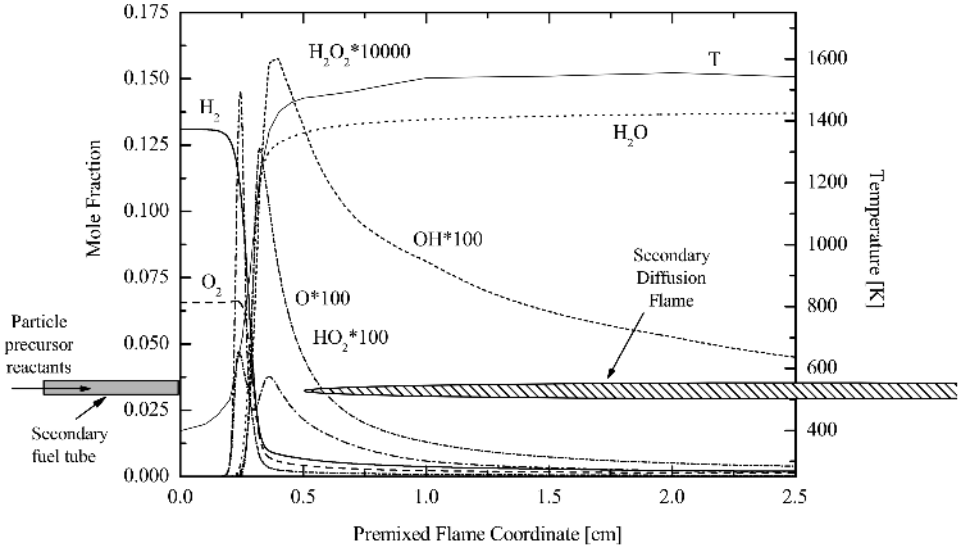

Fig. 8. Calculated species profiles for the primary flame system for typical stoichiometric ($\phi = 1.0$) H_2/O_2/Ar combustion conditions. A sketch of the secondary flame is superimposed on the computational results for reference.

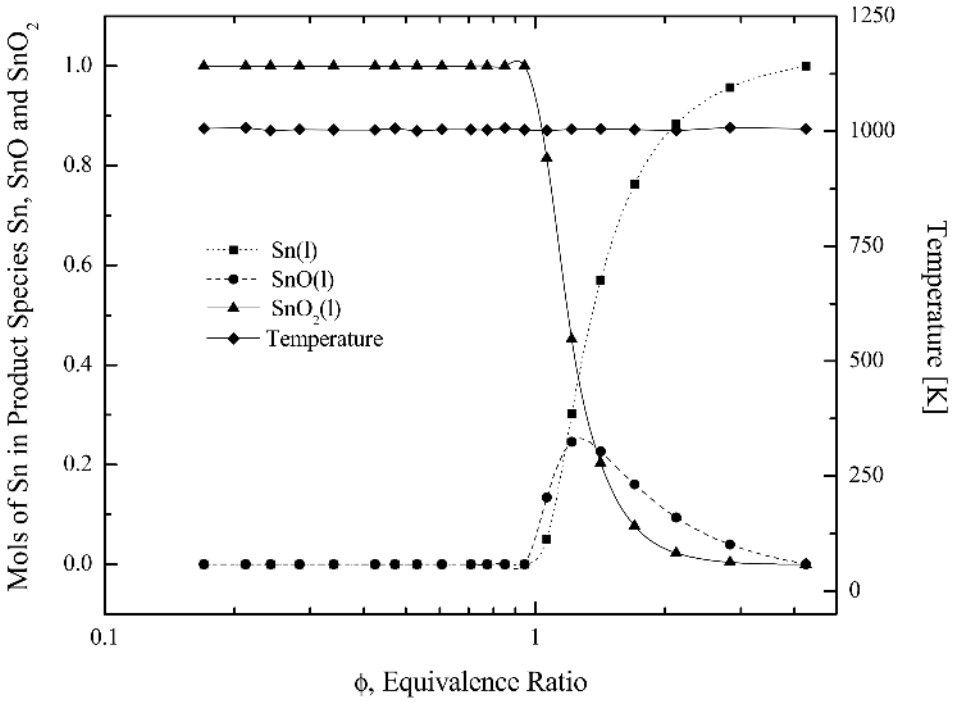

Fig. 9. Equilibrium calculation results of the distribution of Sn in the combustion products of $H_2/O_2/Sn(CH_3)_4/Ar$ flames for $T_{ad} \cong 1000$ K. The results are based on constant reactant values of 1 mol of $Sn(CH_3)_4$ and 1 mol of H_2.

synthesis. Additional details of the model, including the chemical reaction mechanism used, are provided in Donovan *et al.*[34] Again, the chemical kinetics model does not include the effects of the secondary flame, including any chemistry associated with the TMT. As seen in Fig. 8, O_2 is rapidly consumed within 0.5 cm of the surface of the burner by the H_2 in the primary flame.

When both the primary and the secondary flame systems are in use, the secondary flame forms a lifted diffusion flame where the base of the luminous visible portion of the secondary flame is located 5 mm above the surface of the burner. For reference, a schematic of the secondary flame is superimposed on the results in Fig. 8. On exiting the secondary fuel tube, the TMT/Ar gases mix with the O_2 from the surrounding oxidizer channels. However, at typical operating conditions, including $\phi = 1.0$, there is insufficient O_2 in the immediate vicinity of the secondary fuel tube (i.e., the surrounding six oxidizer channels) to completely oxidize the $Sn(CH_3)_4$ to complete products of combustion, i.e., SnO_2, CO_2, and H_2O. Therefore, a potentially significant portion of the TMT and/or Sn and SnO particles (produced in the secondary flame) are likely oxidized by reaction with H_2O—the most abundant oxygen-containing species present in the coannular region surrounding the secondary flame.

Equilibrium calculations which include tetramethyltin and tin species provide additional insight into the chemistry of the $TMT/H_2/O_2/Ar$ system and aid in interpretation of the observed temperature and equivalence ratio dependence to the SnO_x compositions. Figures 9 and 10 present the moles of product tin species as a function of the equivalence ratio for $T_{ad} = 1000$ and 2000 K, respectively. Here, the equivalence ratio is determined using both H_2 and TMT as fuels according to the global reaction

$$Sn(CH_3)_4 + H_2 + xO_2 + y\text{Ar} \rightarrow \text{Products} \quad (2)$$

At stoichiometric conditions, all tin is presumed to form SnO_2, all hydrogen to form H_2O, and all carbon to form CO_2. To separate temperature effects from fuel-to-oxidizer ratio effects, the results of Figs. 9 and 10 are presented for approximately constant temperatures. For all calculations, the fuel loading is maintained at 1 mol of TMT and 1 mol of H_2, the reactants are at 1 atm and 298 K, and the reaction is considered adiabatic. The equivalence ratio is changed by increasing or decreasing the O_2 concentration (x in Reaction 2). The temperature is maintained constant in the calculations by the increasing or decreasing the Ar concentration in the reactants (y in Reaction 2). The reactants, major products of combustion (CO, CO_2, H_2O), some minor products of combustion (H, OH, HO_2, O), and vapor and condensed phases for Sn, SnO, and SnO_2 are considered in the calculations. The thermodynamic data are taken primarily from Cox *et al.*[37] The thermochemical data for TMT are from Allendorf.[38]

Figure 9 shows that $SnO_2(l)$ is the preferred form of tin for low equivalence ratios, whereas at fuel-rich conditions, Sn(l) is preferred. There is a small window in ϕ where SnO(l) is present, but never in quantities above 30% (mole basis) of the initial 1 mol of TMT. However, as the temperature is increased, Fig. 10 shows that SnO(g) is the preferred form of tin for a large range of equivalence ratios. Although the calculations are not directly representative of the synthesis system studied, the trends are in excellent qualitative agreement with the observed dependences on T and ϕ. At higher temperatures and higher fuel concentrations, the O atoms are consumed preferentially by carbon, yielding Sn and SnO products. Conversely, at lower temperatures and fuel-lean conditions, 100% of the TMT is converted to SnO_2.

We are not aware of any previous flame synthesis studies of Sn or SnO; however, the results of the current investigation can be compared on a qualitative basis with other combustion synthesis methods used to produce SnO_2 nanoparticles. It is difficult to compare results on a quantitative basis, due to the limited data available on particle residence time and temperature. Lindackers *et al.* examined SnO_2 synthesis using low-pressure (37.5 mbar), premixed $TMT/H_2/O_2/Ar$ flat flames.[10] The final product powders indexed to the cassiterite phase of SnO_2; however, an intermediate metastable phase (a mixture of the high-temperature β-SnO_2 phase and the α-SnO phase) was also identified in the study. The authors found the powders consisted of primary particles and agglomerates with specific surface areas ranging from ~70 to 160 m^2/g (corresponding to average particle sizes ranging from ~5.5 to 13 nm). Higher TMT loadings led to larger particle sizes, and the highest TMT loading presented in the work was 1348 ppm. The SnO_2 particles produced using the MEDB were larger than those made by Lindackers *et al.*, which is consistent with the atmospheric pressures and the higher TMT loadings (21%–23% mole basis TMT, balance Ar) used in the current work.

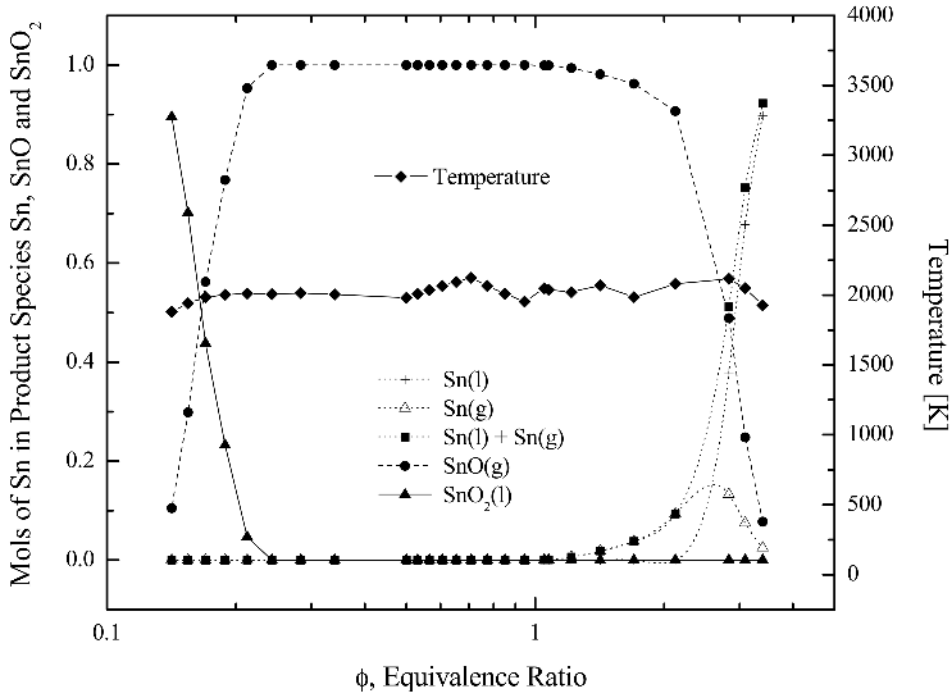

Fig. 10. Equilibrium calculation results of the distribution of Sn in the combustion products of $H_2/O_2/Sn(CH_3)_4/Ar$ flames for $T_{ad} \cong 2000$ K. The results are based on constant reactant values of 1 mol of $Sn(CH_3)_4$ and 1 mol of H_2.

Pratsinis and co-workers studied SnO_2 synthesis using atmospheric pressure coflow diffusion flames[25] and premixed burner-stabilized and premixed burner-nonstabilized flames.[39] For all systems, the SnO_2 particles indexed to cassiterite and were larger than those produced in the current work, with particle sizes determined from specific surface areas ranging from ~52 to 164 nm for the diffusion flames and from ~36 to 65 nm for the premixed flames.

V. Summary and Conclusions

A multielement diffusion burner was successfully used to produce nanocrystalline Sn, SnO, and SnO_2 particles. This is the first demonstration of combustion synthesis of pure metal Sn nanoparticles of which we are aware. The most significant factors controlling particle composition were the concentration of oxygen-containing species locally available for oxidation (primarily O_2 and H_2O) and the temperature of the combustion system. The equilibrium modeling results indicate that the primary flame temperature and equivalence ratio may be used to optimize the synthesis strategy for isolated production of Sn, SnO, or SnO_2 with high reactant-to-product conversion efficiencies (e.g., 1 mol of TMT producing ~1 mol of Sn and little to no SnO or SnO_2). The average particle dimensions (based on specific surface area measurements) were 23–24 nm for the SnO_2 powders produced and 69 nm for the Sn powders produced. The larger Sn particle size is consistent with the more rapid sintering rates of Sn. Note that the Sn particle sizes produced here are substantially smaller than Sn particles made using alternative nanoparticle synthesis methods.

Acknowledgments

The authors thank Dr. Mark D. Allendorf for providing the thermochemical data for $Sn(CH_3)_4$ and Mr. Michael T. Donovan for providing the chemical kinetics modeling results of the primary flame.

References

[1]W. Göpel, "Sensors: A Comprehensive Survey"; Edited by W. Göpel, J. Hesse, and J. N. Zemel. *Chemical and Biochemical Sensors I, II*; Vols. 2–3. Edited by W. Göpel, T. A. Jones, M. Kleitz, I. Lundström, and T. Seiyama. VCH, Weinheim, Germany, 1992.

[2]K. Ihokura and J. Watson, *The Stannic Oxide Gas Sensor—Principles and Applications*. CRC Press, Boca Raton, FL, 1994.

[3]W. Göpel and K. D. Schierbaum, "SnO_2 Sensors: Current Status and Future Prospects," *Sens. Actuators B*, **26–27**, 1–12 (1995).

[4]T. Brousse and D. M. Schleich, "Sprayed and Thermally Evaporated SnO_2 Thin Films for Ethanol Sensors," *Sens. Actuators B*, **31**, 77–79 (1996).

[5]E. Kanazawa, M. Kugishima, K. Shimanoe, Y. Kanmura, Y. Teraoka, N. Miura, and N. Yamazoe, "Mixed Potential Type N_2O Sensor Using Stabilized Zirconia- and SnO_2-Based Sensing Electrode," *Sens. Actuators B*, **75**, 121–24 (2001).

[6]F. E. Krius, H. Fissan, and A. Peled, "Synthesis of Nanoparticles in the Gas Phase for Electronic, Optical and Magnetic Applications—A Review," *J. Aerosol Sci.*, **29** [5–6] 511–35 (1998).

[7]C. Nayral, T. Ould-Ely, A. Maisonnat, B. Chaudret, P. Fau, L. Lescouzères, and A. Peyre-Lavigne, "A Novel Mechanism for the Synthesis of Tin/Tin Oxide Nanoparticles of Low Size Dispersion and of Nanostructured SnO_2 for the Sensitive Layers of Gas Sensors," *Adv. Mater.*, **11** [1] 61–63 (1999).

[8]M. D. Allendorf, "On-Line Deposition of Oxides on Flat Glass," *Electrochem. Soc. Interface*, **10**, 34–38 (2001).

[9]C. J. Giunta, D. A. Strickler, and R. G. Gordon, "Kinetic Modeling of the Chemical Vapor Deposition of Tin Oxide from Dimethyltin Dichloride and Oxygen," *J. Phys. Chem.*, **97**, 2275–83 (1993).

[10]D. Lindackers, C. Janzen, B. Rellinghaus, E. F. Wassermann, and P. Roth, "Synthesis of Al_2O_3 and SnO_2 Particles by Oxidation of Metalorganic Precursors in Premixed H_2/O_2/Ar Low Pressure Flames," *Nanostruct. Mater.*, **10** [8] 1247–70 (1998).

[11]K. C. Song and J. H. Kim, "Synthesis of High Surface Area Tin Oxide Powders via Water-in-Oil Microemulsions," *Powder Technol.*, **107**, 268–72 (2000).

[12]J. Calderer, P. Molinàs, J. Sueiras, E. Llobet, X. Vilanova, X. Correig, F. Masana, and A. Rodríguez, "Synthesis and Characterisation of Metal Suboxides for Gas Sensors," *Microelectron. Reliab.*, **40**, 807–10 (2000).

[13]J. S. Sakamoto, C. K. Huang, S. Surampudi, M. Smart, and J. Wolfenstine, "The Effects of Particle Size on SnO Electrode Performance in Lithium-Ion Cells," *Mater. Lett.*, **33**, 327–29 (1998).

[14]N. Yamazoe, "New Approaches for Improving Semiconductor Gas Sensors," *Sens. Actuators B*, **5**, 7–19 (1991).

[15]C. Xu, J. Tamaki, N. Miura, and N. Yamazoe, "Grain Size Effects on Gas Sensitivity of Porous SnO_2-Based Elements," *Sens. Actuators B*, **3**, 147–55 (1991).

[16]G. Zhang and M. Liu, "Effect of Particle Size and Dopant on Properties of SnO_2-Based Gas Sensors," *Sens. Actuators B*, **69**, 144–52 (2000).

[17]I. Sayago, J. Gutiérrez, L. Arés, J. I. Robla, M. C. Horrillo, J. Getino, J. Rino, and J. A. Agapito, "The Effect of Additives in Tin Oxide on the Sensitivity and Selectivity to NO_x and CO," *Sens. Actuators B*, **26–27**, 19–23 (1995).

[18]P. Siciliano, "Preparation, Characterisation and Applications of Thin Films for Gas Sensors Prepared by Cheap Chemical Method," *Sens. Actuators B*, **70**, 153–64 (2000).

[19]A. Cabot, J. Arbiol, J. R. Morante, U. Weimar, N. Bārsan, and W. Göpel, "Analysis of the Noble Metal Catalytic Additives Introduced by Impregnation of As-Obtained SnO_2 Sol–Gel Nanocrystals for Gas Sensors," *Sens. Actuators B*, **70**, 87–100 (2000).

[20]J. O. Besenhard, J. Yang, and M. Winter, "Will Advanced Lithium-Alloy Anodes Have a Chance in Lithium-Ion Batteries?," *J. Power Sources*, **68**, 87–90 (1997).

[21]J. Santos-Pena, T. Brousse, and D.M. Schleich, "Search for Suitable Matrix for the Use of Tin-Based Anodes in Lithium Ion Batteries," *Solid State Ionics*, **135**, 87–93 (2000).

[22]D. L. Foster, J. Wolfenstine, J. R. Read, and W. K. Behl, "Nanocomposites of Sn and Li_2O Formed from the Chemical Reduction of SnO as Negative Electrode Material for Lithium-Ion Batteries," *Electrochem. Solid State Lett.*, **3** [5] 203–204 (2000).

[23]J. Yang, M. Wachtler, M. Winter, and J. O. Besenhard, "Sub-Microcrystalline Sn and Sn–SnSb Powders as Lithium Storage Materials for Lithium-Ion Batteries," *Electrochem. Solid State Lett.*, **2** [4] 161–163 (1999).

[24]C. G. Borman and R. G. Gordon, "Reactive Pathways in the Chemical Vapor Deposition of Tin Oxide Films by Tetramethyltin Oxidation," *J. Electrochem. Soc.*, **136** [12] 3820–28 (1989).

[25]W. Zhu and S. E. Pratsinis, "Synthesis of SiO_2 and SnO_2 Particles in Diffusion Flame Reactors," *Ceram. Process.*, **43** [11A] 2657–64 (1997).

[26]G. Skandan, N. Glumac, Y.-J. Chen, F. Cosandey, E. Heims, and B. H. Kear, "Low-Pressure Flame Deposition of Nanostructured Oxide Films," *J. Am. Ceram. Soc.*, **81** [10] 2753–56 (1998).

[27]V. M. Jiménez, A. R. González-Elipe, J. P. Espinós, A. Justo, and A. Fernández, "Synthesis of SnO and SnO_2 Nanocrystalline Powders by the Gas Phase Condensation Method," *Sens. Actuators B*, **31**, 29–32 (1996).

[28]L. M. Cukrov, T. Tsuzuki, and P. G. McCormick, "SnO_2 Nanoparticles Prepared by Mechanochemical Processing," *Scr. Mater.*, **44** [8–9] 1787–90 (2001).

[29]K. Brezinsky, "Gas-Phase Combustion Synthesis of Materials," *Proc. Combust. Inst.*, **26**, 1805–16 (1996).

[30]S. E. Pratsinis, "Flame Aerosol Synthesis of Ceramic Powders," *Prog. Energy Combust. Sci.*, **24** [3] 197–219 (1998).

[31]M. S. Wooldridge, "Gas Phase Combustion Synthesis of Particles," *Prog. Energy Combust. Sci.*, **24** [1] 63–87 (1998).

[32]M. S. Wooldridge, P. V. Torek, M. T. Donovan, D. L. Hall, T. A. Miller, T. R. Palmer, and C. R. Schrock, "An Experimental Investigation of Gas-Phase Combustion Synthesis of SiO_2 Nanoparticles Using a Multi-Element Diffusion Flame Burner," *Combust. Flame*, **131** [5] 98–109 (2002).

[33]D. L. Hall, P. V. Torek, C. R. Schrock, T. R. Palmer, and M. S. Wooldridge, "Gas-Phase Combustion Synthesis of Tin Oxide Nanoparticles," *Mater. Sci. Forum*, **386–388**, 347–52 (2002).

[34]M. T. Donovan, D. L. Hall, P. V. Torek, C. R. Schrock, and M. S. Wooldridge, "Demonstration of Temperature and OH Mole Fraction Diagnostic in $SiH_4/H_2/O_2$/Ar Flames Using Narrow Line *UV* OH Absorption Spectroscopy," *Proc. Combust. Inst.*, **29**, 2635–43 (2003).

[35]D. R. Lide (Ed.), *CRC Handbook of Chemistry and Physics*. CRC Press, Boca Raton, FL, 1997.

[36]O. I. Arabi-Katbi, S. E. Pratsinis, P. W. Morrison Jr., and C. M. Megaridis, "Monitoring the Flame Synthesis of TiO_2 Particles by In-Situ FTIR Spectroscopy and Thermophoretic Sampling," *Combust. Flame*, **124** [4] 560–72 (2001).

[37]J. D. Cox, D. D. Wagman, and V. A. Medvedev, Eds., *CODATA Key Values for Thermodynamics*. Hemisphere Publishing Co., New York, 1989.

[38]M. D. Allendorf, personal communication, 2002.

[39]S. Vemury, S. E. Pratsinis, and L. Kibbey, "Electrically Controlled Flame Synthesis of Nanophase TiO_2, SiO_2, and SnO_2 Powders," *J. Mater. Res.*, **12** [4] 1031–42 (1997). □